Modification of a turbulent boundary layer by circular cavities

Francesco Scarano, Marc Jacob, Romain Gojon, Xavier Carbonneau, Erwin Ricky Gowree

Physics of Fluids ARTICLE scitation.org/journal/phf

Modification of a turbulent boundary layer by circular cavities

Cite as: Phys. Fluids **34**, 065134 (2022); doi: 10.1063/5.0091110
Submitted: 11 March 2022 · Accepted: 26 May 2022 ·
Published Online: 16 June 2022

Francesco Scarano,[1,a)] Marc C. Jacob,[2] Romain Gojon,[1] Xavier Carbonneau,[1] and Erwin R. Gowree[1]

AFFILIATIONS

[1]Département Aérodynamique et Propulsion (DAEP) ISAE-SUPAERO, Université de Toulouse, 10, Avenue Edouard Belin 31400, Toulouse, France

[2]Laboratoire de Mécanique des Fluides et d'Acoustique, Ecole Centrale de Lyon, France; Institut National des Sciences Appliquées Lyon, France; and Université Claude Bernard Lyon I, Centre National de Recherche Scientifique, Université de Lyon, 36 av. Guy de Collongue F-69134 Ecully, France

[a)]Author to whom correspondence should be addressed: francesco.scarano@isae-supaero.fr

ABSTRACT

It is shown how well-chosen perforations in a wall flow can locally reduce skin friction drag by modifying the generation of bursts in the boundary layer. For this purpose, a detailed hot wire boundary layer experimental investigation of the flow past a perforated plate, complemented with large eddy simulations, is carried out and compared to the smooth case. The perforated plate is obtained with an array of flush-mounted circular cavities. These cavities are disposed in a periodic staggered arrangement. For the three tested flow velocities, the momentum thickness-based Reynolds number varies from $Re_\theta = 1830$ to 3380 and the cavity diameter and spacing in wall units, respectively, from $d^+ = 130$ to 250 and $L^+ = 587$ to 1075, the latter being identical in both spanwise and streamwise directions. The mean velocity profiles evidence a thickening of the viscous sublayer and a decrease in the friction velocity as compared to the smooth wall case. The application of the Variable Interval Time Averaging technique highlights an upward shift of the bursts from the wall and an attenuation of the average burst intensity and duration. Spanwise measurements evidence an overall bursts attenuation despite the lack of spanwise uniformity. The three-dimensional (3D) mean flow topology arising from the large eddy simulations provides evidence for the qualitative similarities between the current setup and the spanwise wall oscillations.

I. INTRODUCTION

Reducing CO_2 emissions is a major task in civil aviation. The Advisory Council of Aeronautics Research in Europe (ACARE) has recently prescribed a 75% cut in CO_2 emissions per passenger mile with respect to the 2000s level; this target has to be achieved by 2050. Reducing the drag can have a huge impact on the performance and, thus, on the CO_2 emissions reductions. At cruise conditions, in fact, 1% of drag reduction is translated into a 0.75% in fuel-burn savings (Ricco *et al.*, 2021; Leschziner, 2020). The viscous drag is responsible for almost 60% of the total drag at cruise conditions (Ricco *et al.*, 2021; Leschziner, 2020). This component of the drag is mainly due to the turbulent boundary layer developing over the aircraft surfaces.

In turbulent boundary layers, the presence of coherent structures has been largely documented. The so-called hairpin vortex paradigm (Adrian, 2007) can be considered the most complete model of the turbulent coherent structures present in a turbulent boundary layer. This model can explain multiple phenomena, which are responsible for the production of turbulent kinetic energy and increase in skin friction. The hairpin vortices are similar to horseshoe vortices inclined 45° to the wall; they are made of two counter-rotating quasi-streamwise vortices called legs or rolls, which bend toward each other and connect to form the so-called vortex head. The spanwise width of the hairpin is 100 viscous lengths ν/u_τ (where ν is the kinematic viscosity and u_τ is the friction velocity), they are asymmetric, and their streamwise extension is around 1000 viscous lengths (Adrian, 2007). The hairpin vortices are responsible for pumping low momentum fluid away from the wall (ejection) and splashing high momentum fluid close to the wall (sweep) in a process which is called bursting.

Since the pioneering studies by Kline *et al.* (1967), in the region close to the wall, pockets of low momentum have been identified by means of flow visualization. These regions are called streaks, and they are now believed to be associated with the quasi-streamwise vortices, namely, the legs of one or more hairpin vortices (Adrian, 2007). The chaotic oscillation, lift-up, and breakup of the streaks are the so-

called bursting (Robinson, 1991); according to Kline *et al.* (1967), the breakup of the streaks begins at around $Y^+ = 30$. The events contributing to the bursting process can be better understood by the quadrant analysis: these events are ejections ($u < 0$, $v > 0$) also called Q2 and sweeps ($u > 0$, $v < 0$) also called Q4. During a burst, an ejection (when low momentum fluid is pushed away from the wall) is followed immediately by a sweep, which supplies fluid toward the wall. This pattern can be recognized by a single component hot wire signal (Rao *et al.*, 1971). In both cases, the sweeps and the ejections are responsible for the production of the Reynolds shear stress ($-\rho\overline{uv}$) since the product of u and v is negative. The Reynolds shear stress is responsible for accelerating the flow near the wall, which leads to an increase in the mean flow in the vicinity of the wall. As a result, the mean velocity gradient at the wall increases and subsequently the wall shear stress and the skin friction increase (Adrian, 2007).

This whole bursting process plays a crucial role in the production and transport of turbulent energy, the sweep and ejections together are responsible for about 70% of the total shear stress. Almost all the production of turbulent kinetic energy in the wall region of the turbulent boundary layer occurs during a bursting process (Kim *et al.*, 1971). According to Kline *et al.* (1967), there is a linear correlation between the bursts and the skin friction velocity and by consequence viscous drag. In principle, the control and attenuation of the bursting should lead to a reduction in skin friction drag (Leschziner, 2020).

In the last four decades, multiple techniques aiming to reduce the turbulent activity, thus reducing the skin friction, have been developed. The riblets (Walsh, 1980; Choi, 1989) are small fences in the direction of the flow, which restrict the spanwise motion of the rolls, thus hindering the spanwise diffusion of turbulent structures and, hence, reducing the occurrence of sweep events (Jiménez, 2004). This shifts the nature of the process from a direct energy cascade toward an inverse energy cascade, thus increasing the scale on which energy dissipation occurs. In addition, by imposing an offset to the no-slip boundary condition further away from the wall, the riblets are able to move the quasi-streamwise vortices away from the wall lowering the wall shear stress up to 10% (Karniadakis and Choi, 2003; Walsh, 1980). The riblet characteristic sizes (height and spacing between the fences) are usually around 15–20 wall units. According to Walsh and Lindemann (1984), the Reynolds number dependence on the performances of the riblets is due to the change in the friction velocity u_τ, which is reflected in a change of the riblets span-wise spacing in wall units, s^+ (the subscript "+" stands to represent the dimension normalized in wall units); after an optimum value of s^+, the drag further increases.

Another technique to reduce skin friction drag consists in imposing a spanwise oscillating motion on the wall,

$$W(x,t) = A\cos\left(\frac{2\pi}{\lambda_x}x - \frac{2\pi}{T}t\right), \tag{1}$$

where A is the amplitude of the oscillation, λ_x is the wavelength, and T is the period of the oscillation (Ricco *et al.*, 2021; Choi *et al.*, 1998; Quadrio *et al.*, 2009). The spanwise motion imposes a Stokes layer in the spanwise direction, which disrupts the near wall cycle; this, in turn, attenuates the sweeps and ejection, thus reducing the skin friction. According to Karniadakis and Choi (2003), with this technique, a drag reduction up to 40% is possible depending on the flow conditions. There exists a steady version of the technique, introduced by Viotti *et al.* (2009), which has proven to be effective and leads to a considerable drag reduction (up to 52%) by generating a spatial Stokes layer that is able to disrupt the near wall turbulent cycle. From the work by Marusic *et al.* (2021), the drag reduction depends on $\lambda_x^+, A^+, Re_\tau$, and T^+. Multiple studies have been conducted in order to find the optimal parameters; the optimum T^+ is around 100, while drag reduction is documented for wavelengths of $200 < \lambda^+ < 8000$ and for amplitudes A^+ on the order of 10 (Ricco *et al.*, 2021; Di Cicca *et al.*, 2002). The spanwise wall oscillation is an active technique, so trying to reproduce it in real life as well as in laboratories is rather difficult and there exist only a few experimental studies (Auteri *et al.*, 2010 and more recently Marusic *et al.*, 2021) in which the efficacy of spanwise wall oscillation has been proven up to high Reynolds numbers (Re_τ up to 12 800).

Similar techniques that are easier to implement experimentally aim to emulate the effects of spanwise wall oscillations. They consist either in vortex generators (Iuso *et al.*, 2002) or in rotating disks (Ricco and Hahn, 2013). Usually, the scaling of the stream-wise arrangement is very similar to the wavelength of the spanwise wall oscillation, around 550 wall units as reported by Iuso *et al.* (2002).

In the work by van Nesselrooij *et al.* (2016), a skin friction reduction of up to 4% was obtained by the use of staggered dimples; according to the authors, this effect is due to a modification of the turbulent structures that could be associated with a mean flow pattern. The dimples used by van Nesselrooij *et al.* (2016) are shallow (the ratio of boundary layer thickness and the depth of the dimple δ/h is between 5 and 60) and with a large diameter. The diameter scales with the boundary layer thickness with values comprised between $d/\delta = 1.33$ and 4, and the spacing between the dimples varies between 1 and 2.87 diameters. Another experimental study by Tay *et al.* (2015) conducted on a dimpled channel flow (depth to diameter ratios of 1.5% and 5%) documented a drag reduction of up to 3%. It was inferred that dimples are able to generate streamwise vortices, which induce a spanwise flow component near the wall; the effect is a skin friction reduction and a disruption of the turbulence energy cascade suggesting an increase in the streamwise coherence.

Recently, other studies addressed the possibility of having a skin friction reduction and an attenuation of sweep events by means of micro-cavity arrays (Gowree *et al.*, 2019; Silvestri *et al.*, 2017). In the work by Silvestri *et al.* (2017), the reduction of the intensity of the sweep events is documented for certain values of the diameter scaled in wall units ($20 < d^+ < 145$) with an optimum value that corresponds to $d^+ = 60$. According to the authors, this attenuation of the sweeps is linked to the fact that the cavities absorb the sweep events and the associated pressure fluctuations, thus reducing the turbulent activity. Below $d^+ = 20$, the orifices are too small to inject sweeps; above $d^+ = 145$, the shear layer above the cavities can breakup, thus provoking an increase in turbulent kinetic energy near the wall. The spanwise spacing of the cavities was 100 in wall units, and the streamwise spacing was about 1000 to match the dimensions of the coherent structures in a boundary layer. The study conducted by Gowree *et al.* (2019) on three-dimensional circular cavities suggested a possible skin friction drag reduction associated with a critical Reynolds number above which the perforations modify the flow in the near wall resulting in drag rise. The cavities have a staggered pattern that is typical of acoustic liners but different from the arrangement discussed by Silvestri *et al.* (2017).

The aim of the present work is to characterize the turbulent boundary layer grazing over flush-mounted staggered circular cavities. The diameter and depth of the cavities have been chosen in agreement with the previous studies by Gowree *et al.* (2019) and Silvestri *et al.* (2017). The investigation relied on an accurate hot wire boundary layer survey coupled with a careful determination of the wall-to-probe distance. The focus has been put mainly on the investigation of how the cavities modify the turbulent activity and the bursting process. Using the Variable Interval Time Averaging (VITA) technique (Blackwelder and Kaplan, 1976), the profiles of the number of bursts, the burst intensity, and duration have been computed for the perforated surface and the smooth baseline configuration. A limited number of spanwise measurements were conducted downstream of the cavities, and the aim is to verify the uniformity of the modification of the turbulent activity generated by the cavities. The measurement technique was limited in its ability to provide a detailed representation of the three-dimensional flow patterns. Thus, high fidelity Large Eddy Simulations were conducted on a simplified flow domain to complement the experimental finding and infer further details on the skin friction mechanism.

II. METHODOLOGY

A. Experimental setup and procedures

The experimental campaign was conducted in the Sabre wind tunnel at ISAE-SUPAERO, in which the measured turbulence intensity is 0.04% as reported by Chanetz *et al.* (2020). The length of the test section is 2.5 m in the streamwise direction (X), its width is 1.2 m in the horizontal (spanwise) direction (Z), whereas its height is 0.8 m (Y). Inside the test section, a 2.5 m long, 1.2 m wide flat plate is mounted horizontally; the plate has an elliptic leading edge and it is equipped with a flap at the trailing edge. The flap was set at an angle of 3.7° during the entire experimental campaign in order to ensure a zero streamwise pressure gradient along the measurement domain. The acceleration parameter,

$$k_a = \frac{\nu}{U_e^2}\frac{dU_e}{dx}, \tag{2}$$

where U_e is the velocity at the edge of the boundary layer and ν is the kinematic viscosity, is found to be smaller than 1.6×10^{-6} for all the flow conditions, which indicates that the acceleration is not significant and no deviations from the log-law are expected (Patel, 1965). A 400 mm square cut-through is made on the plate to house the test samples, which consisted of either a smooth or a perforated panel. The model centerline is located 600 mm from both sides of the wind tunnel (which corresponds to 30 boundary layer thickness δ); thus, the side effects can be neglected. The slot for the panel is located 1.1 m downstream of the plate leading edge, far enough to have a fully developed turbulent boundary layer along the entire model. The boundary layer is tripped on the flat plate right after the leading edge with a 780 μm wire.

The measurements have been performed using a Dantec 55P15 boundary layer hot wire probe. The operating temperature was around 230° C with an overheat ratio of 1.75. The probe support, stiff enough to avoid vibrations during the acquisition process, has been fixed to a 3 axis traversing system, capable of minimum displacement of 12.5 μm (between 0.33 and 0.61 viscous lengths). In the current experiment, one degree of freedom has been inhibited allowing the measurements only along the vertical plane that coincides with the midspan plane of the model. The hot wire signal was sampled at 20 kHz and filtered analogically by a DISA 55M01 with a cutoff of 10 kHz. King's law was applied for conversion from voltage to velocity, and the hot wire was calibrated *in situ*.

Following the work of Gowree *et al.* (2015), Nikon D5100 equipped with a 300 mm lens and a Kenko Teleconverter 2× have been used for the probe-to-wall alignment and to estimate the probe-wall distance with an accuracy of 9 μm (between 0.23 and 0.44 viscous lengths). This technique proved to be a reliable method to reach the close vicinity of the wall while ensuring that the probe-to-wall distance was accurately estimated and to guarantee that the boundary layer integral quantities were calculated precisely. The probe-to-wall alignment was performed manually; however, the profile scan was performed automatically through LabVIEW. The error associated with the hot wire measurement is evaluated following the method proposed by Jørgensen (2002). The error in the velocity sample is 3.13% with a 95% confidence interval, the error associated with the momentum thickness is 3.55% while the error in the skin friction is 3.5%.

The test samples consist of two square Plexiglas plates of $400 \times 400\,\text{mm}^2$ and 4 mm thickness, one completely smooth and the other with a staggered array of circular cavities [Fig. 1(b)] hereafter referred to as "the perforated model." The use of plexiglass as material for the model reduces the heat transfer effect (with respect to another material such as metal). In addition, the optical probe-to-wall alignment allows checking that the probe is not in contact with the surface. This further reduces the heat transfer effects, which have not been found to be relevant. The back of the perforated model has been sealed, following Gowree *et al.* (2019), in order to avoid interactions between the cavities and the casing gap beneath them. The diameter d of the cavities is 5 mm resulting in a ratio of diameter-to-depth, $d/h = 1.25$ (Fig. 2). The spacing between two cavities on the same row is $L = 22$ mm ($4.4d$), with a stagger angle of 45°. The smooth part upstream of the first row of cavities has been designed in order to recover an unperturbed turbulent boundary layer after the effect of the small gap between the model and the plate, which has been sealed with a 5 μm tape to avoid leakage. The hot wire measurements have been performed at different streamwise locations in the midspan plane of the model. These positions are summarized in Fig. 1(b). The dots represent single velocity profiles taken at the leading edge, middle and trailing edge of both models. The measurements at the leading edge and trailing edge are at one cavity distance L upstream/downstream of the first/last row of cavities. Downstream the last row of cavities (about 20δ downstream of the first row of cavities), the boundary layer is expected to be in full equilibrium with the non-smooth surface (Antonia and Luxton, 1971). After the modification of the traversing system, two spanwise measurements are performed at the trailing edge of the model as part of a second experimental campaign. The spanwise spacing is half of the cavity distance L; in this way, the measurements are in the wake of a cavity (Z_0) between two cavities (Z_+ and Z_-). With the exception of the subsection dedicated to the spanwise measurements, the measurements referred to as the trailing edge will always be in the wake of the cavity (Z_0).

The profiles allow the calculation of the boundary layer thickness δ defined as the value of the normal to wall location Y at which $\bar{U}(Y)$ is equal to 99% of the free-stream velocity U_∞ as well as the

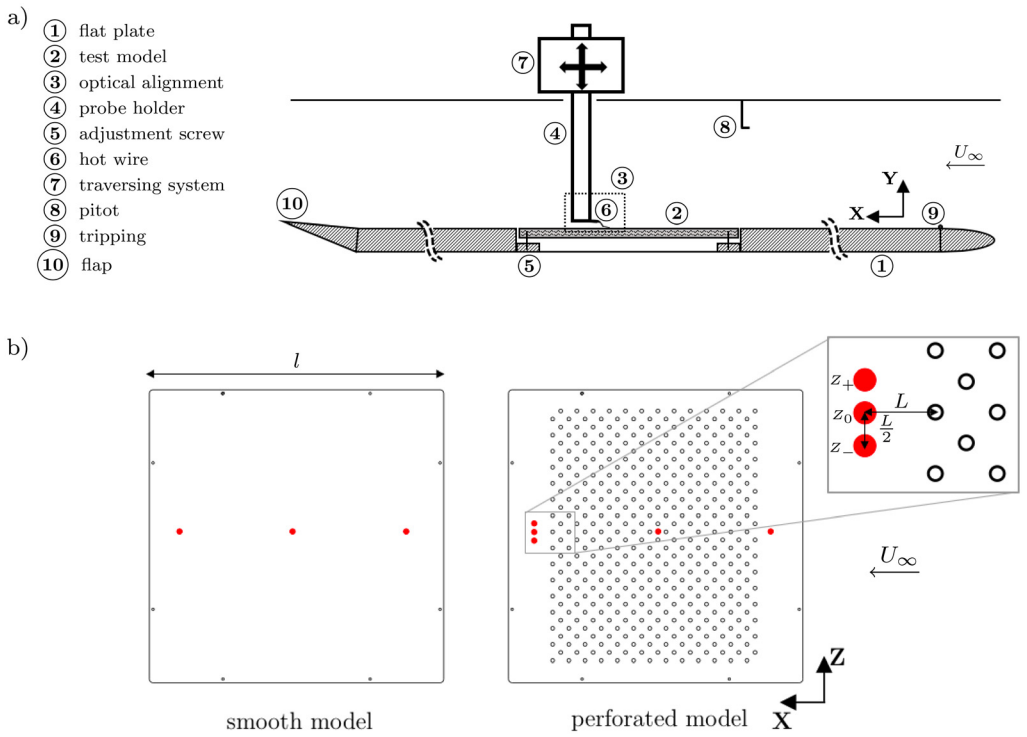

FIG. 1. Sketch of the experimental setup, (a) side cut of the midspan plane and (b) top view of the test models: the red spots indicate the streamwise positions of the vertical velocity profiles in the midspan plane.

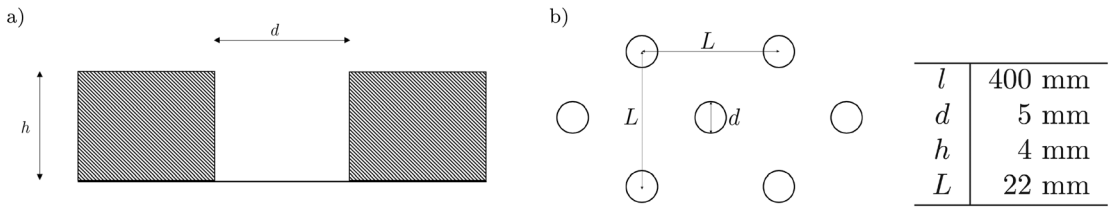

FIG. 2. Details of the cavities dimensions: (a) view from the side and (b) view from the top.

momentum thickness, θ. The Reynolds number based on the momentum thickness, Re_θ, is evaluated at the trailing edge together with other flow parameters as reported in Table I. The tests have been carried out at three velocities: 10, 15, and 20 m/s following the work by Gowree *et al.* (2019). The characteristic dimensions in wall units (d^+, L^+, t^+) change with changing free-stream conditions; the scaling in inner and outer units of the geometrical parameters is reported in Table I. The friction velocity used to compute the geometrical parameters in wall units is obtained on the baseline smooth surface.

Velocity profiles on the smooth model have been sampled through precise scans in the normal to the wall direction assisted by the optical probe-to-wall alignment system. The profiles are then reported in Fig. 3(a) in wall units for three values of Re_θ along with the universal log law,

TABLE I. Flow and geometrical parameters for three different test conditions, downstream measurement location.

CASE	U_∞ (m/s)	$k_a \times 10^{-6}$	Re_θ	Re_d	Re_h	d^+	h^+	Re_τ	L^+	δ/d	δ/h	u_{τ_0}
a)	10	0.013	1830	3165	2530	130	104	580	587	4.3	3.4	0.42
b)	15	0.005	2710	4870	3900	190	152	745	838	3.9	3.1	0.60
c)	20	0.002	3380	6580	5270	250	200	950	1075	3.7	3.0	0.77

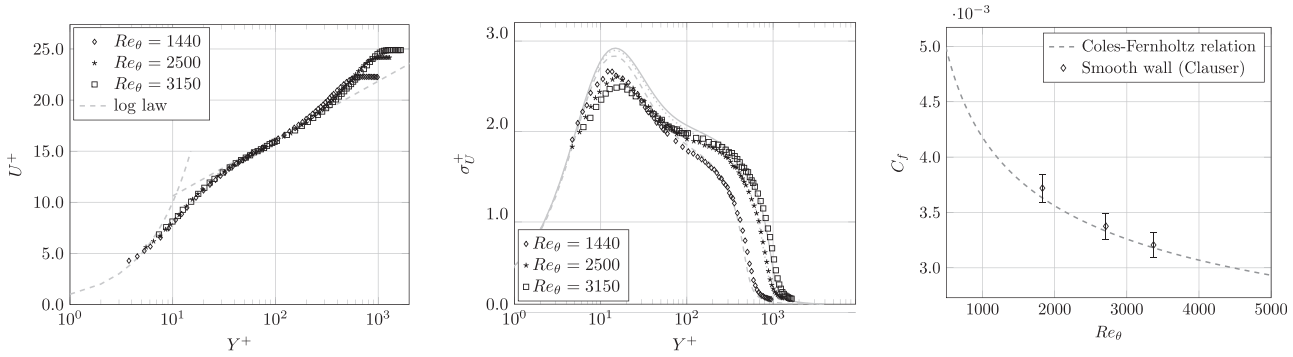

FIG. 3. Smooth model: (a) mean velocity profile in wall units and universal log law in the middle of the model, (b) root mean square in wall units and comparison with data by Schlatter and Orlu (2010) ($Re_\theta = 1420, 2540, 3030$) gray lines, and (c) friction coefficient obtained using the Clauser chart technique and comparison with the Coles–Fernholtz relation.

$$U^+ = \frac{1}{k}\log(Y^+) + B. \tag{3}$$

The profiles are fitted to the Spalding equation following the Clauser chart technique as reported by Kendall and Koochesfahani (2008) using $k = 0.41$ (von Karman constant) and $B = 5.9$ as intercept.

In Fig. 3(b), the profiles of the root mean square of the streamwise velocity fluctuations, σ_U^+, in wall units, are plotted for three different values of Re_θ. The current experimental results are compared with the DNS results of Schlatter and Orlu (2010) in the same range of Reynolds numbers. The current experimental data match well with the numerical data in the wake and the logarithmic regions. When looking at the peak, the trend is opposite to that observed in the numerical simulation (the peak decreases with the Reynolds number), these results are in agreement with the conclusions of Örlü and Alfredsson (2010) who attribute these differences to the limited spatial resolution of the hot wire. In addition, it is worth underlining that the σ_U^+ peak lies at $Y^+ \cong 14$, which is in agreement with values obtained in canonical turbulent boundary layers over flat plates, as reported by Schlatter and Orlu (2010) and Pope (2000). Finally, the turbulent spectra, reported in Fig. 15 at the trailing edge of the model, confirm that the boundary layer can be considered fully developed.

When dealing with moderately thick turbulent boundary layers, as in the present case, where very few points inside the viscous sublayer are measured, the evaluation of the skin friction by a linear fit in the viscous sub-layer is challenging. Thus, the friction coefficient is calculated with the Clauser chart technique (Wei *et al.*, 2005). In Fig. 3(c), the friction coefficient is plotted against Re_θ for the baseline model and compared with the Coles-Fernholtz relation (see Schlichting and Gersten, 2017) showing a good match.

III. RESULTS

A. Boundary layer profiles

In Figs. 4 and 5, the mean and RMS (Root Mean Square) velocity profiles in the middle of the model and downstream the last row of cavities are plotted in wall units and compared with the corresponding smooth results. The profiles are plotted for increasing flow velocities from left to right: since the momentum thickness is not conserved between the two models, the velocities are referred to by their associated non-dimensional perforation diameters d^+ (140, 190, and 250) that correspond to the smooth model Re_θ values indicated in Table I (1830, 2710, and 3380). The profiles have been fitted to the Spalding equation following the Clauser chart technique (Wei *et al.*, 2005; Kendall and Koochesfahani, 2008). An upward shift of the buffer and the logarithmic region of the mean profile starts to occur in the middle of the model, and it is more evident downstream of the cavities; this is true for all the flow conditions. Downstream of the cavities this shift is more pronounced at $d^+ = 130$ and decreases when increasing the free-stream velocity. A similar shift, usually associated with a thickening of the viscous sub-layer (see Lumley, 1973), has been largely reported in the literature, and it is associated with a drag reduction by means of riblets (Choi, 1989), spanwise wall oscillations (Di Cicca *et al.*, 2002; Choi *et al.*, 1998), and large scale streamwise vortices (Iuso *et al.*, 2002).

In agreement with Silvestri *et al.* (2017), the σ_U^+ peak of the perforated model at the trailing edge is about 5% lower with respect to the smooth baseline and the peak is slightly shifted toward higher values of Y^+. This behavior is valid for all the flow conditions, and it is present but less evident even for the measurement in the middle of the model. For $d^+ = 250$, an increase in the RMS can be observed at about $Y^+ \cong 100$. In the wake region, the RMS profiles obtained for the smooth and perforated model tend to collapse, suggesting that the outer layer is only slightly affected by the cavities.

The local friction velocity downstream of the last row of cavities is calculated by fitting the Spalding equation following the Clauser chart technique (Wei *et al.*, 2005; Kendall and Koochesfahani, 2008). The same technique has been used by Gowree *et al.* (2019) and Silvestri *et al.* (2017) for similar investigations. In Fig. 6, the local skin friction reduction percentage between the perforated and baseline surface is reported. A local skin friction reduction (respectively, 14.5%, 13.8%, and 11%) can be observed for all the freestream conditions but a decrease in the skin friction reduction with d^+ can be evidenced; similar trends are reported in the studies by Gowree *et al.* (2019) and Silvestri *et al.* (2017).

The percentage variation between the momentum thicknesses of the perforated and smooth walls at the downstream location is evaluated and plotted against the Reynolds number based on the cavity diameter Re_d and the cavity depth Re_h. The results reported in Figs. 7(a) and 7(b)

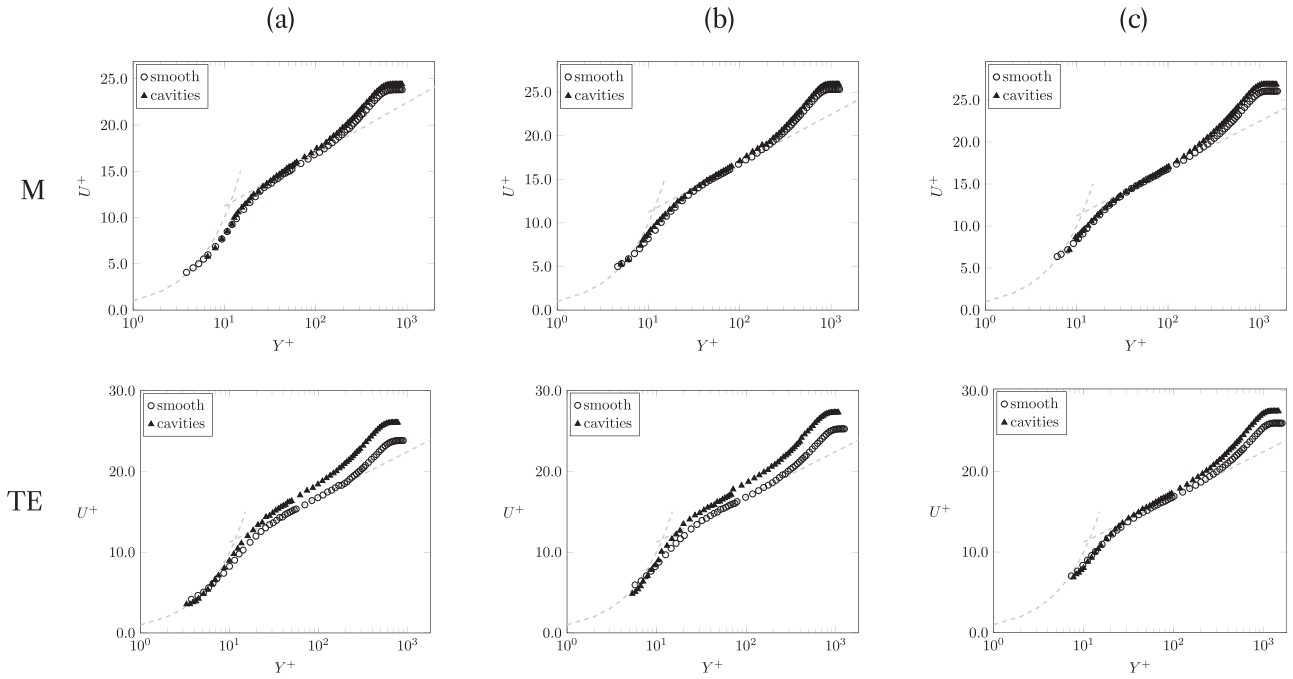

FIG. 4. Mean velocity in wall units in the middle and trailing edge of the model: (a) $d^+ = 130$, (b) $d^+ = 190$, and (c) $d^+ = 250$.

show, respectively, a close resemblance to the results obtained by Gowree *et al.* (2019) for similar flow conditions and similar geometrical parameters of the model (diameter, spacing, and thickness); this provides some confidence with regard to the reproducibility of the experiment in a different environment and with a different test model. In addition, this consolidates the fact that the momentum thickness variation is strongly correlated with the Reynolds number based on the cavity diameter.

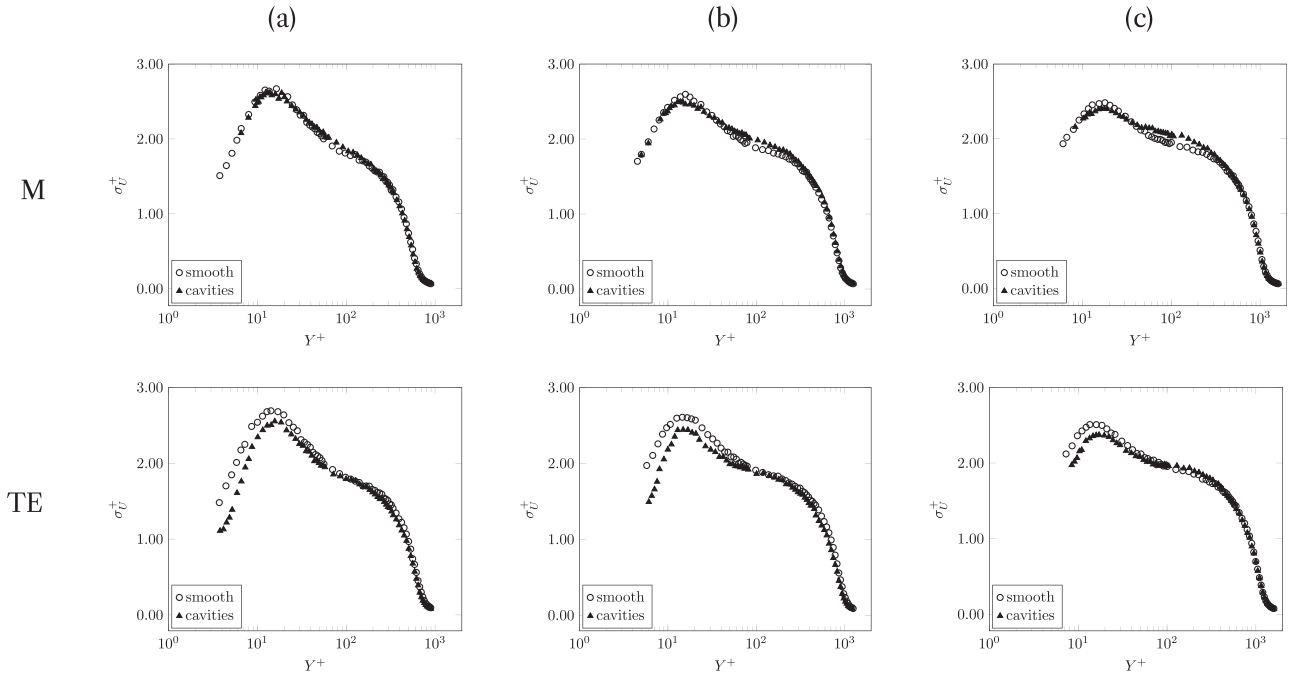

FIG. 5. Root mean square of the streamwise velocity in wall units in the middle and trailing edge of the model: (a) $d^+ = 130$, (b) $d^+ = 190$, and (c) $d^+ = 250$.

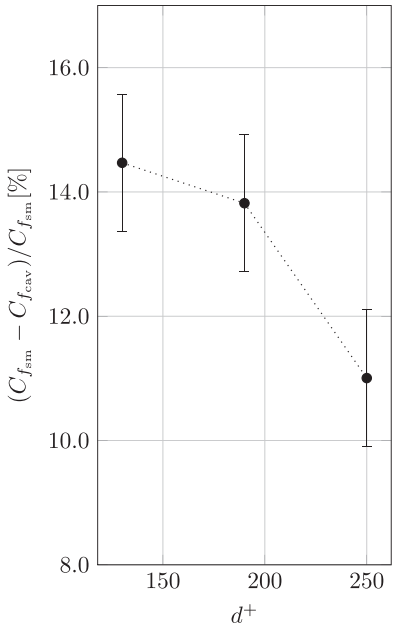

FIG. 6. Percentage skin friction reduction obtained using the Clauser chart technique.

B. VITA analysis

The Variable Interval Time Averaging (VITA) has been used to characterize the turbulent activity in the presence of the cavities. This technique, first proposed by Blackwelder and Kaplan (1976), is a simple and powerful way to detect shear events, which can be associated with bursts in a turbulent boundary layer.

Given a fluctuating quantity $Q(x_i, t)$, the short-term average of the variable in the interval time T can be defined as

$$\widehat{Q}(x_i, t, T) = \int_{t-\frac{T}{2}}^{t+\frac{T}{2}} Q(x_i, s)ds. \tag{4}$$

In order to obtain an average that is representative of a short event, it is fundamental to choose a physically consistent value of T. Blackwelder and Kaplan (1976) and Sullivan and Pollard (1996) proposed to choose this parameter based on the friction time $T^+ = \frac{Tu_\tau^2}{\nu}$ with T^+ between 10 and 20, representative of the duration of a burst event, which corresponds to about 70 and 30 samples depending on the free-stream condition (and by consequence on the friction velocity). The standard procedure is to apply the local mean to the square of the local mean streamwise velocity and subtract the local mean square value,

$$\widehat{\mathrm{var}}(x_i, t, T) = \widehat{U^2}(x_i, t, T) - \left[\widehat{U}(x_i, t, T)\right]^2. \tag{5}$$

The detection is then based on a Heaviside function,

$$D(t) = \begin{cases} 1 & \text{if } \widehat{\mathrm{var}}(x_i, t, T) > k \cdot \sigma_U^2, \\ 0 & \text{otherwise,} \end{cases} \tag{6}$$

where σ_U is the root mean square of the total record of the signal. In other words, short-term RMS peaks relative to the long-time RMS of the signal, defines burst events (see Sullivan and Pollard, 1996). A threshold level k on the VITA variance signal has to be applied to detect the event. The choice of this parameter is crucial for the detection; following the study of Blackwelder and Kaplan (1976), a value between $k = 0.8$ and $k = 1.2$ has been chosen presently.

1. Number of bursts

The application of the VITA technique leads to a profile with the number of bursts detected through the boundary layer. The friction velocity used to compute the time window as well as Y^+ is the actual friction velocity for each case. This can be used to confront the burst

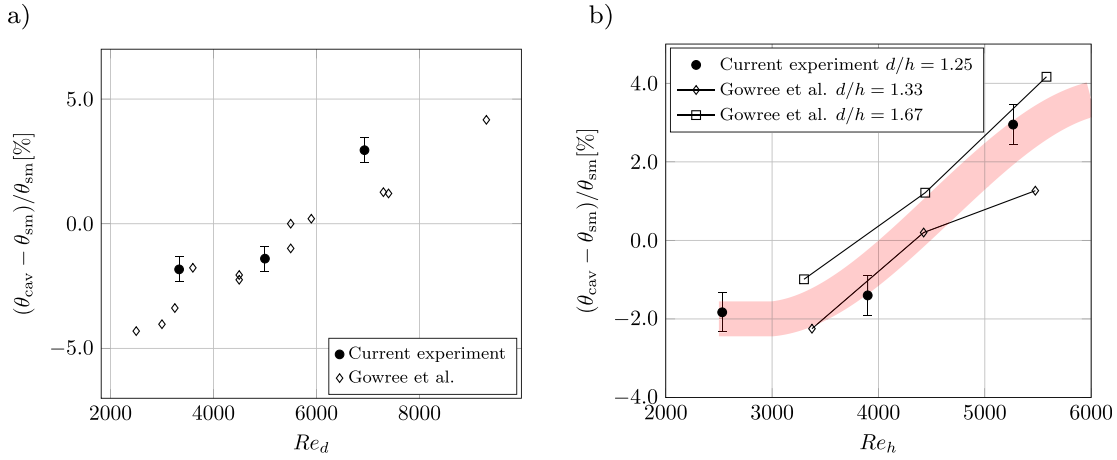

FIG. 7. Momentum thickness percentage variation between the perforated and smooth surface. (●) present measurements at the trailing edge, (□) and (◇) Gowree *et al.* (2019), considering only results for similar *d*/*h*. (a) Evolution with the Reynolds number based on the cavity diameter and (b) evolution with the Reynolds number based on the cavity depth.

profiles above the smooth to those above the perforated wall; this should give an indication of how the turbulent activity is modified in the presence of the cavities. As expected, the shape of a burst profile for the smooth condition is dominated by the presence of a bump with a peak in the region $10 < Y^+ < 20$, as reported by Blackwelder and Kaplan (1976) or Jasinski and Corke (2020). A comparison between the smooth and perforated walls in the middle of the model is reported in Fig. 8 for $k = 1$ and $T^+ = 15$. Figure 8 shows that the burst profiles in the smooth configuration are similar for the three flow conditions, while the number of detections for each sample is different due to different time windows that depend on the friction velocity. In the perforated configuration, in the middle of the model, a shift toward higher values of Y^+ can be identified for all the test velocities, namely, for all the values of d^+. The results for the downstream profiles, instead, evidence no shift of turbulence activity, suggesting that this behavior does not persist on the smooth part downstream of the cavities as opposed to the mean flow modification.

The burst profile can be seen as a qualitative way to look at the distribution of the turbulent kinetic energy along the boundary layer. A shift of the burst peak would suggest an upward displacement of the turbulent activity. This shift toward higher values of Y^+, documented previously by Iuso *et al.* (2002), can be associated with a near-wall turbulent cycle and regeneration modification. As postulated by Choi *et al.* (1998) and Di Cicca *et al.* (2002) for span-wise flow oscillations, a reorganization of the turbulent structures leads to a shift of the stream-wise vortices that are pushed away from the wall and generate a lower value of wall shear stress leading to a skin friction drag benefit.

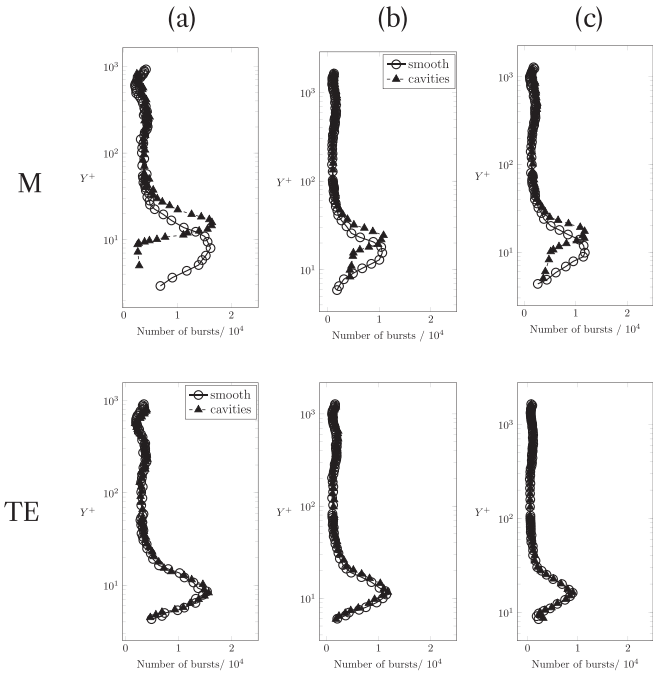

FIG. 8. Burst profiles in the middle and trailing edge of the model, comparison with the smooth baseline, (a) $d^+ = 130$, (b) $d^+ = 190$, and (c) $d^+ = 250$, $k = 1$ and $T^+ = 15$.

It is important to underline that, in contradiction with the studies of drag reduction by means of large-scale stream-wise vortices, conducted by Iuso *et al.* (2002), the burst frequency does not reduce when the drag reduction mechanism is present; on the contrary, a slight increase in the peak frequency ($\cong 1\%$) is reported for the drag reduction conditions, which is in line with studies on riblets by Choi (1989), which is surprisingly at first glance, given the difference between riblets and the present perforations: this aspect deserves to be examined in more detail. The most significant effect, however, is the shift toward higher values of Y^+ in the middle of the model, which is about $\Delta Y^+ \cong 5$ for the three flow conditions. In Fig. 9, the upward shift in the middle of the model remains quite constant while varying the VITA parameters k and T^+ over a limited range of values. According to Choi *et al.* (1998) and Di Cicca *et al.* (2002), a displacement of the turbulent events outwards from the wall, as a consequence of the effect of span-wise wall oscillations, is reflected by a thickening of the viscous sub-layer and an upward shift of the logarithmic velocity profiles: this is an indicator of a reorganization of the turbulent structures in the inner region. According to Choi *et al.* (1998), in fact, the viscous sub-layer went up to $Y^+ \cong 2.5$ for the uncontrolled case and up to $Y^+ \cong 10$ for the case with maximum drag benefit; their measurements were taken right downstream of the manipulated surface ($\Delta X^+ \cong 70$ from the end of the manipulated surface). Their results are in good agreement with respect to what is shown in Fig. 9 for different free-stream conditions. It is noticeable that this shift decreases slightly when increasing the free-stream velocity, namely, the d^+.

2. Average bursts intensity

The conditionally sampled events at a given value of Y^+ can be averaged to obtain an average burst event; the average bust intensity is then defined as the peak-to-peak value of the detected event (see Silvestri *et al.*, 2017). The results shown in Fig. 10 are the measurements relative to the trailing edge of the panel and are obtained for $T^+ = 15$ and $k = 1$ but, even in this case, changing the VITA parameters has little effect on the results. On the right column of Fig. 10, a comparison of the average intensity profile of the perforated case and the smooth baseline is reported; on the left column, the average events at $Y^+ \cong 20$ are presented. For all flow conditions, the cavities reduce the intensity of the bursts in the region $20 < Y^+ < 80$. Interestingly, as can be seen from the conditioned event in Fig. 10, even if the burst slope is reduced in the region where the intensity reduction is obtained, the results have been omitted for brevity. For the sake of completeness, the intensity profiles for the middle of the model are reported in Fig. 11. They show similar results with respect to the ones at the trailing edge apart from the $d^+ = 250$, where at $Y^+ \cong 20$, a larger reduction is achieved compared to the value at the trailing edge.

The profiles of the relative intensity reduction have been computed for each flow condition and plotted in Fig. 12 in the middle of the model and at the trailing edge. Due to different values of Y^+ between the perforated and smooth baselines, the data have been interpolated and the relative intensity differences for a fixed value of Y^+ have been computed. The intensity reduction is most pronounced in the region $20 < Y^+ < 80$ (blue) with a relative reduction up to about 20% for $d^+ = 130$. For the $d^+ = 130$ case, both for the middle and the trailing edge, the reduction covers even the region $90 < Y^+ < 200$. In the middle of the model for $d^+ = 250$, an

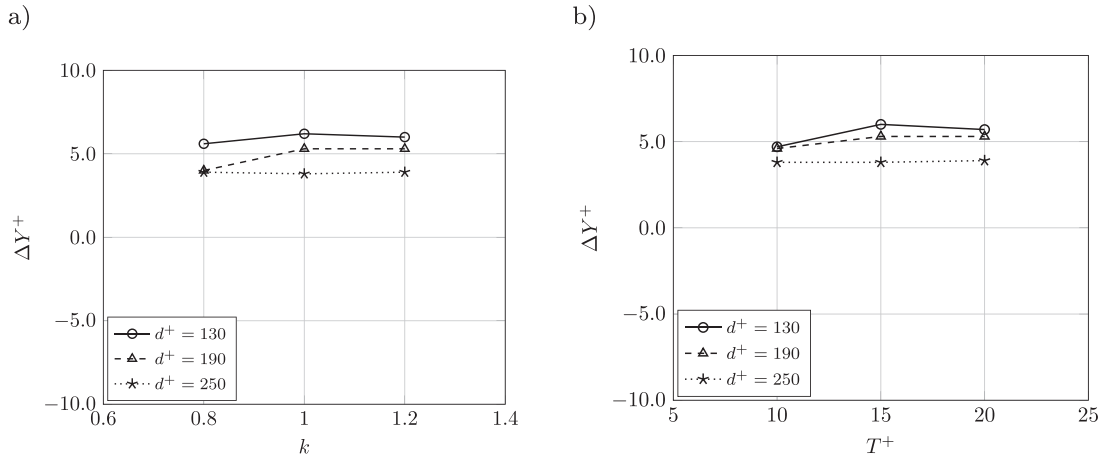

FIG. 9. Shift of the burst frequency peak $\Delta Y^+ = Y^+_{cav} - Y^+_{sm}$ in the middle of the model when changing the VITA parameters: (a) k ($T^+ = 15$) and (b) T^+ ($k = 1$).

intensity reduction of about 10%, with respect to the value at the trailing edge that is about 5%, is achieved.

It is possible to plot the intensity reduction against d^+ at a fixed value of Y^+. From Fig. 13, one can notice that the current results match well the trend with d^+ reported by Silvestri *et al.* (2017) for $Y^+ = 100$, for the results obtained at the trailing edge. Small differences in the intensity reduction can be due to the different parameters used for the VITA technique, imperfections of the cavities, or the intrinsic chaotic nature of the phenomenon. The current results at lower values of Y^+ ($20 < Y^+ < 80$), not reported by Silvestri *et al.* (2017), as well as the average in the region $0 < Y^+ < 200$ evidence a decrease in intensity, namely, a positive intensity reduction, even for the values of d^+, which have been considered above the limit for skin friction reduction.

A region where the burst intensity is reduced can be observed both in the middle of the model and at the trailing edge. These results are valid for all the d^+ tested in this work, therefore, for all the three flow conditions. In the same region of the boundary layer ($20 < Y^+ < 80$), most of the Reynolds shear stress and the turbulent kinetic energy are produced by the lift-up and breakup of the streaks during the bursting process (Kline *et al.*, 1967). This means that a reduction of the burst intensity in that region can be associated with a damping of the sweeps and ejections, thus generating a reduction of the Reynolds shear stress, which, in turn, provokes a reduction of the turbulent mixing close to the wall and a decrease in the mean velocity gradient at the wall. This explanation further corroborates the local skin friction reduction obtained using the Clauser chart technique and reported in Sec. III A. However, this hypothesis has to be further confirmed by Reynolds shear stress measurements.

3. Average bursts duration

From the conditionally sampled average event, the profile of the average duration of the bursts is computed by considering the time interval between the two peaks in the intensity of the conditionally sampled burst. The duration profiles of the perforated vs the smooth case are shown in Fig. 14 for each flow configuration. The burst duration profile has a lobe in correspondence of $5 < Y^+ < 20$, where the maximum of the duration is evidenced for all the flow conditions around $Y^+ \cong 10$. For the position in the middle of the model, a significant duration reduction is reported for all the three flow conditions tested. Such a pronounced effect of the cavities on the burst duration does not persist at the trailing edge.

Here, a slight decrease in the duration of the bursts is identifiable for the perforated case with respect to the smooth baseline; this reduction is more pronounced for $d^+ = 130$. This shows that the burst duration at the trailing edge is marginally affected as such by the perforations and does not occur at the position of maximum intensity. The perforations seem to shift this position slightly toward the wall as observed in plots (a) and (c) but not in plot (b).

C. Turbulent power spectra

The premultiplied power spectra of the streamwise velocity fluctuations at the trailing edge are presented for the three flow conditions in Fig. 15. The spectra are computed using the Welch algorithm with 98 segments having each a window size of 2^{11} samples and no overlap.

The premultiplied spectra are non-dimensionalized with the friction velocity obtained from the smooth baseline model and are shown for the normal to wall location of $Y^+ \cong 30$, where the peak of the burst intensity reduction is achieved for all the flow conditions (see Fig. 12). These results suggest that the cavities reduce the kinetic energy associated with the streamwise turbulent fluctuations. Once again these results can be seen as a further confirmation of the fact that the cavities dampen the streak breakup, thus mitigating the burst process and leading to a turbulent skin friction reduction.

Finally, it is important to recall that for all the Y^+ and the streamwise locations considered, no noticeable shift of the spectra toward lower frequencies occurs. This contradicts the studies by Iuso *et al.* (2002) and Tay *et al.* (2015) who report a considerable skin friction reduction that they relate to a shift of the turbulent spectrum toward the lower frequencies, which indicates an energy increase in the large scale structures.

D. Spanwise measurements

A set of measurements that includes velocity profiles at various spanwise locations is presented here. For the sake of brevity, only the

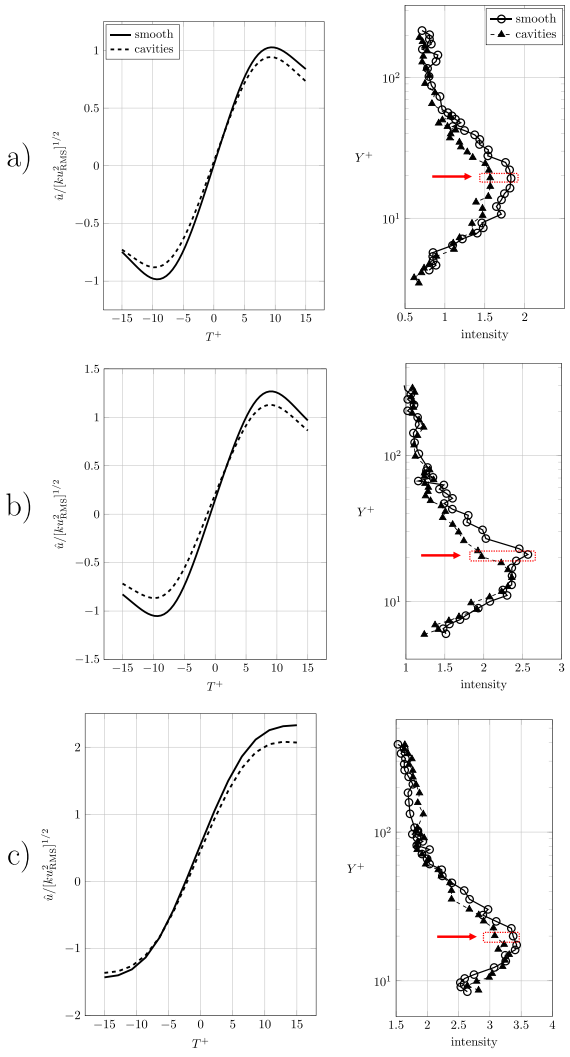

FIG. 10. Comparison between the smooth and the perforated configuration of conditional sampled burst $Y^+ \cong 20$ at the trailing edge of the panel (left) and profile of the burst intensity for the three flow conditions: (a) $d^+ = 130$, (b) $d^+ = 190$, and (c) $d^+ = 250$, $T^+ = 15, k = 1$.

intensity profiles are reported. Similar conclusions can be drawn about the coefficients associated with the spanwise profiles calculated using the Clauser chart technique.

From Fig. 16(a) ($d^+ = 130$), a decrease in the burst intensity is reported for the Z_0 measurement (blue line) confirming the results reported in Fig. 10. The intensity reduction is less pronounced for the two other spanwise measurements. The measurements at Z_+ and Z_- closely match apart from the peak, which is slightly shifted. When averaging the intensity profile, Fig. 16(b), an overall intensity decrease is still perceptible (about 8% for $20 < Y^+ < 40$) less than what is obtained directly downstream of a cavity (about 20%, see Fig. 12). This behavior is observed for all the flow conditions tested as illustrated in Fig. 16(c), which displays the spanwise average intensity profile for $d^+ = 250$.

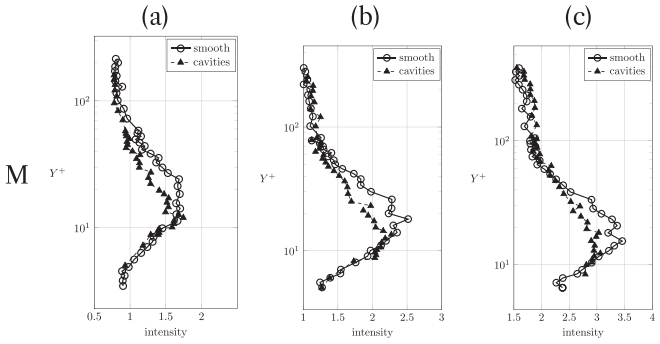

FIG. 11. Profiles of the burst intensity for the three flow conditions in the middle of the model: (a) $d^+ = 130$, (b) $d^+ = 190$, and (c) $d^+ = 250$, $T^+ = 15, k = 1$.

E. Three-dimensional topology from LES

With the objective to complement the experimental results, a series of numerical simulations have been carried out. The aim is to reproduce the effect of the cavities on the mean flow for further insight into the flow in the vicinity and within the cavity, which was limited by the hot wire technique. The three-dimensional (3D) results arising from the numerical simulations were also meant to allow the analysis of the spanwise evolution of the mean flow over a short distance, not achievable during the experiment.

The solver, which had already been successfully applied to turbulent flows over airfoils (Grébert *et al.*, 2016; Boukharfane *et al.*, 2019) and to shock boundary layer interactions (Grébert *et al.*, 2017, 2018), performs wall-resolved large eddy simulations using an explicit time-stepping and the subgrid scale model of Vreman (2004). The geometry reproduces the 3D region corresponding to two rows of cavities, the

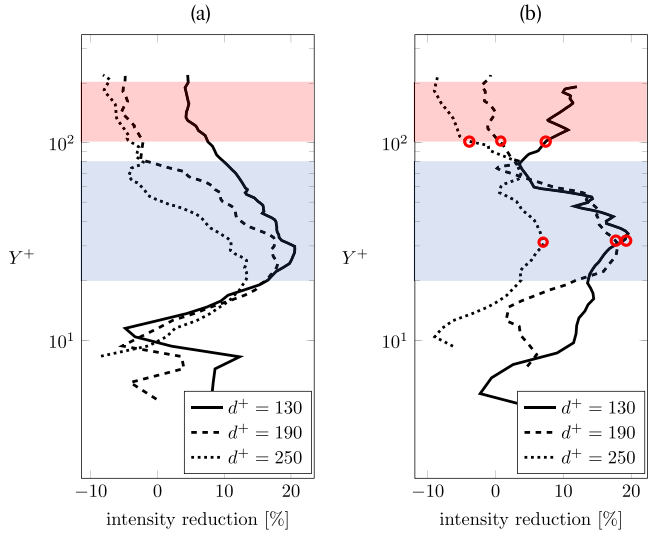

FIG. 12. Profiles of the burst intensity reduction with respect to the smooth baseline: (a) middle of the model, (b) trailing edge, red dots correspond to $Y^+ = 30$ and $Y^+ = 100$, the blue rectangle to $20 < Y^+ < 80$ and the red rectangle to $100 < Y^+ < 200$, $T^+ = 15, k = 1$.

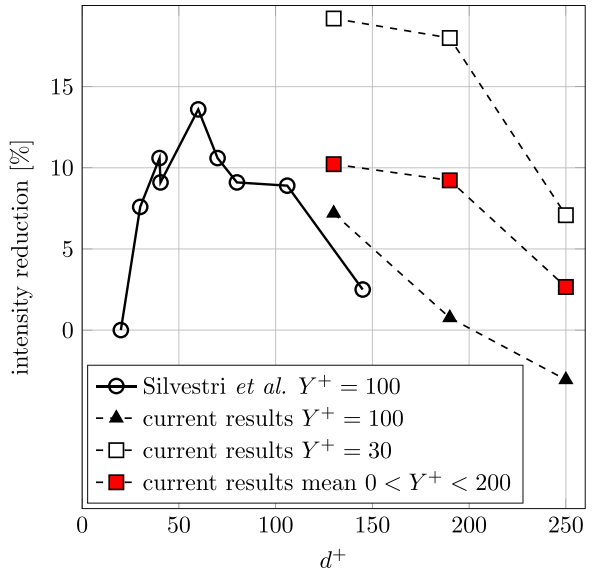

FIG. 13. Burst intensity reduction as a function of d^+ at different Y^+, comparison with Silvestri *et al.* (2017), $T^+ = 15, k = 1$.

first row being located one diameter downstream of the inlet. The dimensions of the cavities and their arrangement have been kept identical to the experimental model. A periodic boundary condition has been imposed in a spanwise direction every $4.4d$. A 2D unstructured extruded mesh in the normal-to-wall direction has been designed using the open-source software GMSH (Geuzaine and Remacle, 2009) resulting in a final mesh count of 6×10^6 hexahedral cells. The mesh has been refined near the wall and in the cavities: the maximal distance-to-wall of the first velocity point is $Y^+ = 1$.

The wall-resolved mean velocity profiles obtained experimentally on the smooth surface slightly upstream of the cavities for the three tested free-stream velocities have been imposed as inlet conditions. No synthetic turbulence has been added to the inlet velocity: the aim is to study the effect of the cavities on the mean flow only. This approach, already undertaken for similar investigations (Bauerheim and Joly, 2020), allows a huge reduction in the computational costs but has the drawback of not being fully representative of the incoming turbulence field. This means that a quantitative comparison of the statistical field or the turbulent boundary layer quantities with the experimental data was not possible. In addition, due to the numerical geometry that includes only the three first rows of cavities, the skin friction cannot be compared with the experimental results. Nevertheless, the numerical simulations provide interesting complementary data, although a

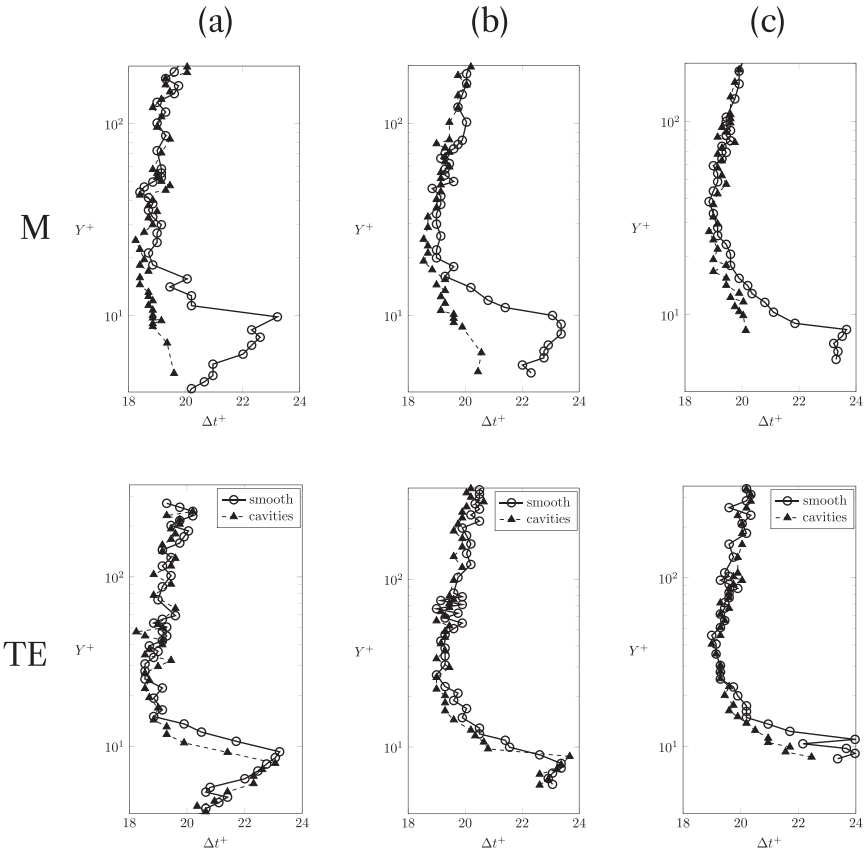

FIG. 14. Burst duration profiles in the middle and trailing edge of the model, comparison with the smooth baseline, (a) $d^+ = 130$, (b) $d^+ = 190$, and (c) $d^+ = 250$.

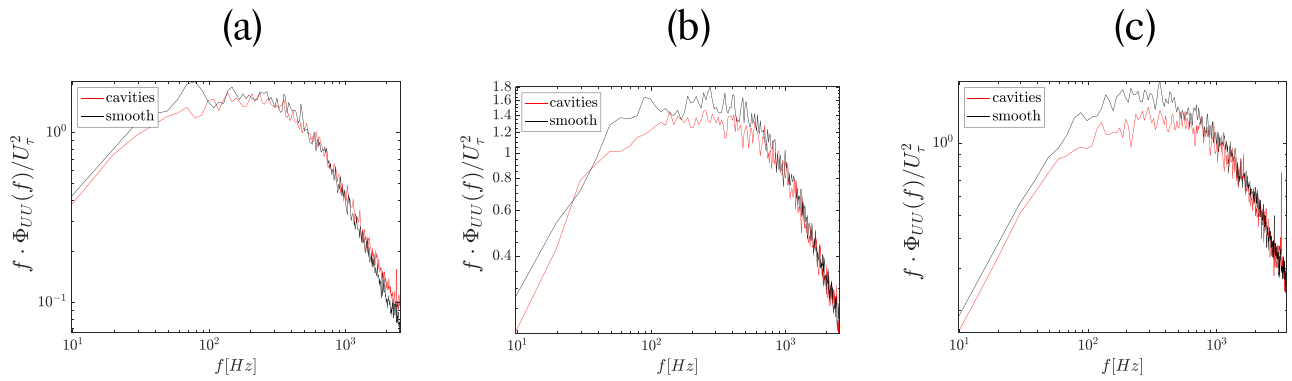

FIG. 15. Spectra of the stream-wise velocity fluctuations at $Y^+ \cong 30$ in the trailing edge (bottom): (a) $d^+ = 130$, (b) $d^+ = 190$, and (c) $d^+ = 250$.

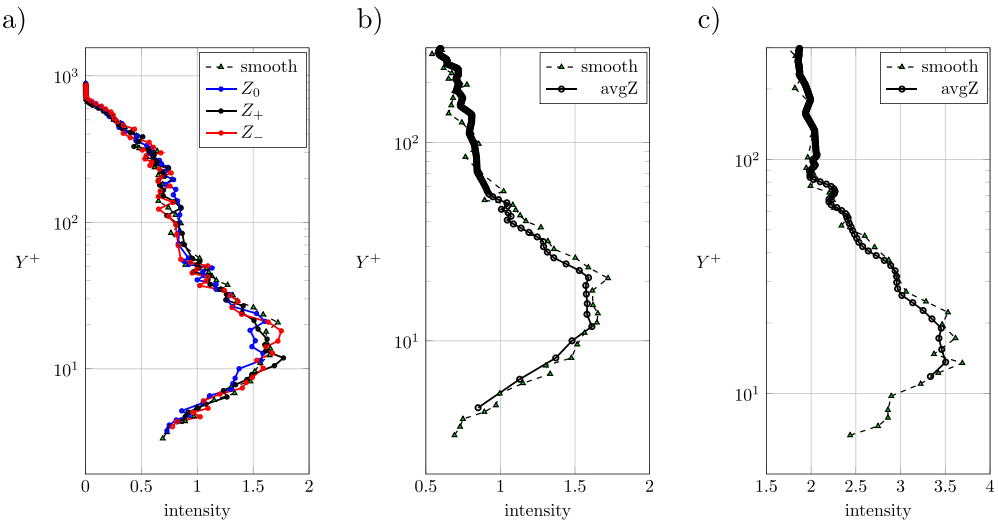

FIG. 16. Intensity profiles, comparison with the smooth baseline, (a) different spanwise locations $d^+ = 130$, (b) spanwise average intensity profile for $d^+ = 130$, and (c) spanwise average intensity profile for $d^+ = 250$.

proper quantitative comparison is not possible due to the absence of turbulence in the incoming boundary layer.

As shown in Fig. 17, each cavity produces 3D flow perturbations in the cavity itself and its vicinity. The curved geometry of the cavity leads the flow to accelerate and curve on the sides. The flow then rolls down inside the cavity generating a counter-rotating vortex. This structure is responsible for flow recirculation. The vortex then induces a positive vertical velocity component V and the formation of another structure downstream of the cavity. The presence of similar structures inside and over dimples for certain flow regimes has been already documented in the literature (see van Nesselrooij *et al.*, 2016; Lienhart *et al.*, 2008).

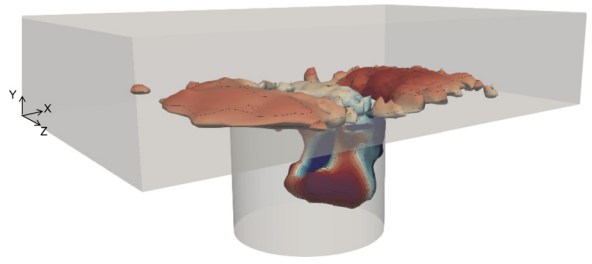

FIG. 17. Iso-surface of the Q-criterion at $d^+ = 130$, colored by the contour of $V/U_\infty \times 100$ from -5% (blue) to 5% (red).

The curvature of the stream-lines on the two sides of each cavity is responsible for the generation of an alternating spanwise mean velocity pattern that resembles a checkerboard. In Fig. 18(a), a slice at $Y^+ \cong 5$ of the contour of the non-dimensional spanwise mean velocity at 10 m/s is presented. This pattern has the spanwise and stream-wise periodicity of the spacing L between the cavities. This phenomenon is present for the three inflow conditions tested. The magnitude of this spanwise velocity is on the order of 1% of the free-stream velocity. This percentage decreases by 13% when the flow velocity is raised to 20 m/s.

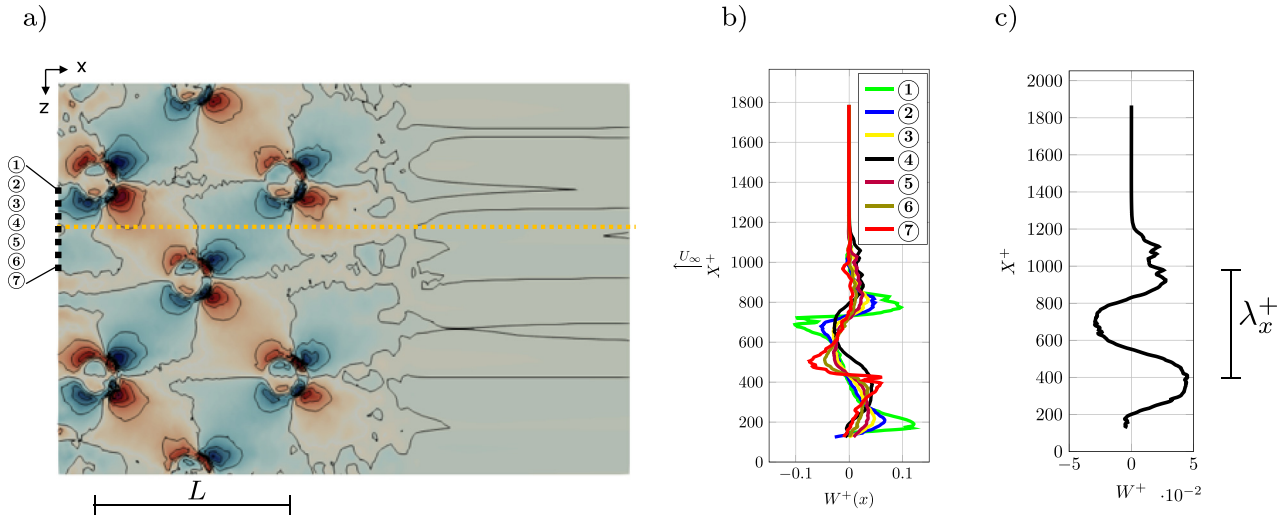

FIG. 18. Flow topology at $d^+ = 130$, (a) contour of W/U_∞[%], slice normal to the wall at $Y^+ \cong 5$, contour from −1% (blue) to 1% (red), (b) evolution of $W(x)$ at seven different spanwise locations between the cavities, and (c) evolution of $W(x)$ along the yellow dotted line (X, $Y^+ = 5, Z = L/2$) as shown in (a).

The streamwise evolution of the spanwise mean velocity at different spanwise locations is reported in Figs. 18(b) and 18(c) along the yellow line ($X, Y^+ = 5, Z = L/2$) shown on plot (a). Figure 18(c) shows a qualitative similarity with the evolution resulting from a near wall steady spanwise oscillation introduced by Viotti *et al.* (2009).

This similarity is purely based on the observation of the mean flow topology from the LES results and by the fact that similar turbulence behavior is obtained from the experimental data. In the work by Viotti *et al.* (2009), a "stationary distribution of spanwise velocity that alternates in the streamwise direction" is imposed directly at the wall. Here, the cavities would then generate a spanwise velocity modulation that has the following form:

$$W^+(x) = A^+ \cos\left(\frac{2\pi}{L^+}x\right). \tag{7}$$

The wavelength of the oscillation is equal to the cavity distance ($\lambda_x^+ = L^+$) and is in agreement with the range in which spanwise oscillations are effective in reducing drag ($200 < \lambda^+ < 8000$). The main differences with respect to the results reported by Viotti *et al.* (2009) and to other unsteady wall oscillations (Ricco *et al.*, 2021) lie in the two orders of magnitude difference in oscillation amplitude in wall units. The other waveforms [Fig 18(b)], which at some spanwise location (e.g., Ref. 7), have even a larger amplitude than the sinusoidal waveform, resemble the non-sinusoidal periodic forcing investigated by Cimarelli *et al.* (2013), which outperform the sinusoidal shape in drag reduction even for smaller amplitudes.

Surface flow visualizations by Gowree *et al.* (2019) evidenced spanwise velocities and curved streamlines, which are in agreement with the current numerical findings. The attenuation of the oscillation amplitude with d^+ is in agreement with the decrease in skin friction reduction found experimentally. This suggests again that the drag reduction properties could be linked to the geometrical parameters of the cavities (diameter, depth) as well as the freestream conditions. The amplitude depends on the strength and the coherence of the vortex inside the cavity, which, in turn, possibly depends on the ratio between the impinging boundary layer thickness and the cavity depth.

The presence of a spanwise flow component and the resulting three-dimensional flow features are known to reduce the Reynolds shear stress and, consequently, the turbulent skin friction drag. A spanwise flow, in fact, can displace the near wall longitudinal vortices and the streaks, thus disrupting the near wall cycle, the streak breakup mechanism and so the whole bursting process (Viotti *et al.*, 2009; Choi, 2002). Viotti *et al.* (2009) stressed that the steady spanwise wall oscillation may be generated passively by some sort of well-designed roughness.

IV. DISCUSSION AND CONCLUSIONS

The present study aims to investigate the modification of the turbulent boundary layer by flush-mounted circular cavities disposed in a staggered arrangement similar to Gowree *et al.* (2019). The characteristic dimensions of the cavity array (namely, the diameter, the depth, and the spacing) in wall units are changed along with the free-stream conditions. The cavity diameter is chosen in agreement with Gowree *et al.* (2019); the values of the diameter in wall units lie in the range, where in the work by Silvestri *et al.* (2017), the turbulent attenuation is expected to decrease.

Confidence in the measurements is a result of the accurate probe-to-wall alignment (Gowree *et al.*, 2015), which gave satisfactory results for a similar study (Gowree *et al.*, 2019). Moreover, for the smooth baseline, a good match with the canonical turbulent boundary layer is found. The boundary layer surveys confirmed the possibility of reducing the turbulent activity, resulting in local skin friction reduction. A thickening of the viscous sublayer, as well as a reduction of the friction velocity, computed using the Clauser chart technique, and a decrease in σ_U^+ confirms the reduction in skin friction. According to previous work on cavities (Silvestri *et al.*, 2017; Gowree *et al.*, 2019), the drag due to the pressure distribution in the cavities should not overcome the benefit from the skin friction drag savings. This

reduction is mitigated when the Reynolds number and d^+ are increased as found by Silvestri *et al.* (2017) and Gowree *et al.* (2019).

The VITA analysis allowed a more detailed characterization of the turbulent activity. The number of burst profiles in the middle of the model show a systematic upward shift, where the burst frequency peak is shifted by $\Delta Y^+ \cong 5$. This is in agreement with the thickening of the boundary layer and has been previously found for drag reduction achieved by means of spanwise oscillations (Iuso *et al.*, 2002; Choi *et al.*, 1998; Di Cicca *et al.*, 2002). Even though the thickening of the viscous sublayer is more visible at the trailing edge, the profiles of the number of burst match one of the smooth baselines, suggesting that the burst frequency modifications do not persist downstream of the cavities. Similar considerations can be made for the duration profiles: the significant reduction of the duration does not persist at the trailing edge of the model.

In both the middle and trailing edge of the model, the average intensity of the bursts decreases, with two distinct regions in the profiles. In the first region ($100 < Y^+ < 200$), the intensity reduction decreases with d^+ and becomes negative for $d^+ = 190$ and $d^+ = 250$. On contrary, when considering the second region that is closer to the wall ($20 < Y^+ < 80$), although the intensity reduction decreases with d^+, an intensity reduction is achievable even for the largest d^+. This is true even when considering the mean intensity reduction in the region $0 < Y^+ < 200$, suggesting that an intensity reduction is possible even for higher values of d^+ at least for the current configuration.

These modifications in burst activities would suggest a reduction of local skin friction drag. The region where the intensity decrease is more pronounced, at $20 < Y^+ < 80$, is where most of the Reynolds shear stress and the turbulent kinetic energy are produced by the streak instability and breakup. A decrease in intensity and duration of the bursts would suggest a reduction of the Reynolds shear stress with a consequent influence on the mean flow, which, in turn, would lead to a skin friction reduction. This picture is further confirmed by the premultiplied spectra that showed a decrease in the energy associated with the streamwise velocity fluctuations in the region of the boundary layer where the intensity reduction occurs.

According to Silvestri *et al.* (2017), the mechanism responsible for the reduction in burst intensity relies on the disruption of the bursting process that is a consequence of the partial or complete penetration of the sweep inside the cavities. A small diameter $d^+ < 20$ would inhibit this effect while a larger diameter $d^+ > 145$ would lead to a breakup of the shear layer. To further explain the skin friction reduction mechanism, numerical simulations have been carried out. The mean flow topology revealed that the cavities passively generate a spanwise checkerboard flow pattern. The streamwise evolution of the spanwise velocity is similar to that obtained by imposing spanwise steady wall oscillations as reported by Viotti *et al.* (2009). The passive creation of a spanwise flow pattern could, in fact, be an alternative explanation for the current findings with respect to that proposed by Silvestri *et al.* (2017). This hypothesis is in line with the explanation that is given for the drag reduction by dimples (van Nesselrooij *et al.*, 2016; Tay *et al.*, 2015). Vortical structures and spanwise velocities similar to those reported herein are, in fact, mentioned in the work of Lienhart *et al.* (2008) for dimples in which a slight skin friction reduction is reported. The decrease in the performance can be due to a coherence loss of the vortical structure inside the cavities. Similar changes in the regime are reported for dimples (van Nesselrooij *et al.*, 2016).

One of the main limitations of the study of Silvestri *et al.* (2017) is related to the lack of spanwise measurements. LDA measurements at various spanwise locations conducted by Gowree *et al.* (2019) evidenced that there is only a weak spanwise variation of the mean velocity profiles suggesting that the drag benefit is not just local in the wake of the cavities. A limited number of spanwise measurements revealed that the turbulent activity is not homogeneous in the spanwise direction. In particular, the measurements out of the cavity wake of the cavities (Z_+ and Z_-) evidence a smaller burst intensity decrease. However, what has to be underlined is that the spanwise average burst intensity profiles still show an overall and non-negligible intensity reduction with respect to the smooth baseline. This is encouraging because it confirms that the attenuation of turbulent activity is not just a local phenomenon in the wake of the cavities.

A limitation of this study lies in the lack of a parametric study, and the design is such that the characteristic dimensions in wall units change when changing the flow velocity. It is, therefore, not possible to separate the effects of changing the dimensions in wall units and changing the impinging boundary layer parameters (such as the boundary layer thickness). Extensions of this study could focus on understanding the effect of the cavity spacing, diameter, and impinging boundary layer parameters in order to provide further insight into the drag reduction mechanism.

ACKNOWLEDGMENTS

The research leading to these results received funding from AID (Agence Innovation Défense) under Grant Agreement No. 2019 65 0028 for the FriDa (Skin Friction Drag of Perforated Acoustic Surfaces) project. The numerical work was performed using HPC (high performance calculus) resources from GENCI (Grand Équipement National De Calcul Intensif)-IDRIS (Institut du développement et des ressources informatiques) and GENCI-CINES (Centre Informatique National de l'Enseignement Supérieur) on Jean Zay, Occigen (Grant No. A0082A07178), and CALMIP (Calcul en Midi-Pyrénées Mésocentre de Calcul) on Olympe (Grant No. 2020-p1425). We also thank Rémy Chanton and Henri Dedieu for their technical support during the experimental campaign.

AUTHOR DECLARATIONS

Conflict of Interest

The authors have no conflicts to disclose.

Author Contributions

Francesco Scarano: Conceptualization (lead); Data curation (lead); Formal analysis (lead); Investigation (lead); Methodology (lead); Visualization (lead); Writing – original draft (lead). **Marc C. Jacob:** Formal analysis (supporting); Funding acquisition (equal); Investigation (equal); Methodology (supporting); Project administration (equal); Supervision (equal); Validation (equal); Visualization (equal); Writing – review & editing (equal). **Romain Gojon:** Software (lead). **Xavier Carbonneau:** Supervision (supporting). **Erwin R. Gowree:** Conceptualization (supporting); Formal analysis (supporting); Funding acquisition (equal); Investigation (supporting); Project administration (equal); Resources (equal); Supervision (equal);

Validation (equal); Visualization (equal); Writing – review & editing (equal).

DATA AVAILABILITY

The data that support the findings of this study are available from the corresponding author upon reasonable request.

REFERENCES

Adrian, R. J., "Hairpin vortex organization in wall turbulence," Phys. Fluids **19**(4), 041301 (2007).

Antonia, R. A., and Luxton, R. E., "The response of a turbulent boundary layer to a step change in surface roughness part 1. Smooth to rough," J. Fluid Mech. **48**(4), 721–761 (1971).

Auteri, F., Baron, A., Belan, M., Campanardi, G., and Quadrio, M., "Experimental assessment of drag reduction by traveling waves in a turbulent pipe flow," Phys. Fluids **22**(11), 115103 (2010).

Bauerheim, M., and Joly, L., "LES of the aero-acoustic coupling in acoustic liners containing multiple cavities," in AIAA Aviation Forum, 2020.

Blackwelder, R. F., and Kaplan, R. E., "On the wall structure of the turbulent boundary layer," J. Fluid Mech. **76**(1), 89–112 (1976).

Boukharfane, R., Bodart, J., Jacob, M., Joly, L., Bridel-Bertomeu, T., and Node-Langlois, T., "Characterization of the pressure fluctuations within a controlled-diffusion airfoil boundary layer at large Reynolds numbers," in 25th AIAA/CEAS Aeroacoustics Conference, 2019.

Chanetz, B., Délery, J., Gilliéron, P., Gnemmi, P., Gowree, E., and Perrier, P., *Experimental Aerodynamics – An Introductory Guide,* 1st edition (Springer, 2020).

Choi, K., "Near-wall structure of a turbulent boundary layer with riblets," J. Fluid Mech. **208**, 417–458 (1989).

Choi, K.-S., "Near-wall structure of turbulent boundary layer with spanwise-wall oscillation," Phys. Fluids **14**(7), 2530–2542 (2002).

Choi, K.-S., DeBisschop, J.-R., and Clayton, B. R., "Turbulent boundary-layer control by means of spanwise-wall oscillation," AIAA J. **36**(7), 1157–1163 (1998).

Cimarelli, A., Frohnapfel, B., Hasegawa, Y., De Angelis, E., and Quadrio, M., "Prediction of turbulence control for arbitrary periodic spanwise wall movement," Phys. Fluids **25**(7), 075102 (2013).

Di Cicca, G. M., Iuso, G., Spazzini, P. G., and Onorato, M., "Particle image velocimetry investigation of a turbulent boundary layer manipulated by spanwise wall oscillations," J. Fluid Mech. **467**, 41–56 (2002).

Geuzaine, C., and Remacle, J.-F., "Gmsh: A 3D finite element mesh generator with built-in pre- and post-processing facilities," Int. J. Numer. Methods Eng. **79**(11), 1309–1331 (2009).

Gowree, E., Atkin, C., and Gruppetta, S., "A simple digital-optical system to improve accuracy of hot-wire measurements," Meas. Sci. Technol. **26**, 095303 (2015).

Gowree, E., Jagadeesh, C., and Atkin, C., "Skin friction drag reduction over staggered three dimensional cavities," Aerosp. Sci. Technol. **84**, 520–529 (2019).

Grébert, A., Bodart, J., Jamme, S., and Joly, L., "Simulations of shock wave/turbulent boundary layer interaction with upstream micro vortex generators,"in 10th International Symposium on Turbulence and Shear Flow Phenomena, 2017.

Grébert, A., Bodart, J., Jamme, S., and Joly, L., "Simulations of shock wave/turbulent boundary layer interaction with upstream micro vortex generators," Int. J. Heat Fluid Flow **72**, 73–85 (2018).

Grébert, A., Bodart, J., and Joly, L., "Investigation of wall-pressure fluctuations characteristics on a naca0012 airfoil with blunt trailing edge," AIAA Paper No. AIAA 2016-2811, 2016.

Iuso, G., Onorato, M., Spazzini, P. G., and Di Cicca, G. M., "Wall turbulence manipulation by large-scale streamwise vortices," J. Fluid Mech. **473**, 23–58 (2002).

Jasinski, C, and Corke, T., "Mechanism for increased viscous drag over porous sheet acoustic liners," AIAA J. **58**(0), 3393–3404 (2020).

Jiménez, J., "Turbulent flows over rough wall," Annu. Rev. Fluid Mech. **36**, 173–196 (2004).

Jørgensen, F., "How to measure turbulence with hot-wire anemometers—A practical guide," in *Dantec Dynamics - Technical Guide* (2002).

Karniadakis, G. E., and Choi, K., "Mechanisms on transverse motion in turbulent wall flows," Annu. Rev. Fluid Mech. **35**(1), 45–62 (2003).

Kendall, A., and Koochesfahani, M., "A method for estimating wall friction in turbulent wall-bounded flows," Exp. Fluids **44**, 773–780 (2008).

Kim, H. T., Kline, S. J., and Reynolds, W. C., "The production of turbulence near a smooth wall in a turbulent boundary layer," J. Fluid Mech. **50**(1), 133–160 (1971).

Kline, S. J., Reynolds, W. C., Schraub, F. A., and Runstadler, P. W., "The structure of turbulent boundary layers," J. Fluid Mech. **30**(4), 741–773 (1967).

Leschziner, M. A., "Friction-drag reduction by transverse wall motion—A review," J. Mech. **36**(5), 649–663 (2020).

Lienhart, H., Breuer, M., and Köksoy, C., "Drag reduction by dimples?—A complementary experimental/numerical investigation,"in the Fifth International Symposium on Turbulence and Shear Flow Phenomena (TSFP5) [Int. J. Heat Fluid Flow **29**(3), 783–791 (2008)].

Lumley, J. L., "Drag reduction in turbulent flow by polymer additives," J. Polym. Sci. Macromol. Rev. **7**(1), 263–290 (1973).

Marusic, I., Chandran, D., Rouhi, A., fu, M., Wine, D., Holloway, B., Chung, D., and Smits, A., "An energy-efficient pathway to turbulent drag reduction," Nat. Commun. **12**, 5805 (2021).

Örlü, R., and Alfredsson, P.-H., "On spatial resolution issues related to time-averaged quantities using hot-wire anemometry," Exp. Fluids **49**, 101–110 (2010).

Patel, V. C., "Calibration of the preston tube and limitations on its use in pressure gradients," J. Fluid Mech. **23**(1), 185–208 (1965).

Pope, S. B., Turbulent Flows (Cambridge University Press, 2000).

Quadrio, M., Ricco, P., and Viotti, C., "Streamwise-travelling waves of spanwise wall velocity for turbulent drag reduction," J. Fluid Mech. **627**, 161–178 (2009).

Rao, K. N., Narasimha, R., and Narayanan, M. A. B., "The 'bursting' phenomenon in a turbulent boundary layer," J. Fluid Mech. **48**(2), 339–352 (1971).

Ricco, P., and Hahn, S., "Turbulent drag reduction through rotating discs," J. Fluid Mech. **722**, 267–290 (2013).

Ricco, P., Skote, M., and Leschziner, M. A., "A review of turbulent skin-friction drag reduction by near-wall transverse forcing," Prog. Aerosp. Sci. **123**, 100713 (2021).

Robinson, S. K., "Coherent motions in the turbulent boundary layer," Annu. Rev. Fluid Mech. **23**(1), 601–639 (1991).

Schlatter, P., and Orlu, R., "Assessment of direct numerical simulation data of turbulent boundary layers," J. Fluid Mech. **659**, 116–126 (2010).

Schlichting, H., and K. Gersten, edited by *Boundary-Layer Theory* (Springer, Berlin/Heidelberg, 2017).

Silvestri, A., Ghanadi, F., Arjomandi, M., Cazzolato, B., and Zander, A., "Attenuation of sweep events in a turbulent boundary layer using micro-cavities," Exp. Fluids **58**, 1–13 (2017).

Sullivan, P., and Pollard, A., "Coherent structure identification from the analysis of hot-wire data," Meas. Sci. Technol. **7**(10), 1498–1516 (1996).

Tay, C., Khoo, B., and Chew, Y., "Mechanics of drag reduction by shallow dimples in channel flow," Phys. Fluids **27**, 035109 (2015).

van Nesselrooij, M., Veldhuis, L. L. M., van Oudheusden, B. W., and Schrijer, F. F. J., "Drag reduction by means of dimpled surfaces in turbulent boundary layers," Exp. Fluids **57**(9), 142 (2016).

Viotti, C., Quadrio, M., and Luchini, P., "Streamwise oscillation of spanwise velocity at the wall of a channel for turbulent drag reduction," Phys. Fluids **21**(11), 115109 (2009).

Vreman, A., "An eddy-viscosity subgrid-scale model for turbulent shear flow: Algebraic theory and applications," Phys. Fluids **16**(10), 3670–3681 (2004).

Walsh, M., and Lindemann, A., "Optimization and application of riblets for turbulent drag reduction," in AIAA 22nd Aerospace Sciences Meeting, Reno, NV, 9–12 January 1984 (AIAA, 1984).

Walsh, M. J., "Drag characteristics of V-groove and transverse curvature riblets," in *Conference Proceedings: Symposium on Viscous flow drag reduction* (1980).

Wei, T., Schmidt, R., and Mcmurtry, P., "Comment on the Clauser chart method for determining the friction velocity," Exp. Fluids **38**, 695–699 (2005).